

Chandra X-ray Observations of the Young Stellar Cluster NGC 6193 in the Ara OB1 Association

S.L. Skinner^{1*}, S.A. Zhekov^{2,3}, F. Palla⁴, and C.L.D.R. Barbosa⁵

¹*CASA, Univ. of Colorado, Boulder, CO 80309-0389 USA*

²*JILA, Univ. of Colorado, Boulder, CO 80309-0440 USA*

³*On leave from Space Research Institute, Moskovska str. 6, Sofia-1000, Bulgaria*

⁴*INAF-Osservatorio Astrofisico di Arcetri, Largo E. Fermi 5, 50125 Firenze, Italy*

⁵*Instituto de Astronomia, Geofísica e Ciências Atmosféricas, Universidade de São Paulo, Rua do Matão 1226, 05508-900 São Paulo, SP, Brazil*

Accepted 2005 April 25. Received 2005 March 7; in original form 2005 March 7.

ABSTRACT

A 90 ksec *Chandra* HETG observation of the young stellar cluster NGC 6193 in the southern Ara OB1 association detected 43 X-ray sources in a $2' \times 2'$ core region centered on the massive O stars HD 150135 (O6.5V) and HD 150136 (O3 + O6V). The cluster is dominated by exceptionally bright X-ray emission from the two O stars, which are separated by only $10''$. The X-ray luminosity of HD 150136 is $\log L_X = 33.39$ (ergs s⁻¹), making it one of the most luminous O-star X-ray sources known. All of the fainter X-ray sources in the core region have near-IR counterparts, but existing JHK photometry provides little evidence for near-IR excesses. These core sources have typical mean photon energies $\langle E \rangle \approx 2$ keV and about one-third are variable. It is likely that some are young low-mass stars in the cluster, but cluster membership remains to be determined. Grating spectra show that the X-ray properties of HD 150135 and HD 150136 are similar, but not identical. Both have moderately broadened unshifted emission lines and their emission is dominated by cool plasma at $kT \approx 0.3$ keV, pointing to a wind-shock origin. However, the emission of HD 150136 is slightly hotter and four times more luminous than its optical twin HD 150135. We discuss the possibility that a radiative colliding wind shock contributes to the prodigious X-ray output of the short-period (2.66 d) spectroscopic binary HD 150136. A surprising result is that the X-ray emission of HD 150136 is slowly variable on a timescale of <1 day. The origin of the variability is not yet known but the observed behavior suggests that it is an occultation effect.

Key words: open clusters and associations: individual (NGC 6193, Ara OB1) – stars:formation – stars: early-type – stars: individual (HD 150135, HD 150136) – X-rays:stars.

1 INTRODUCTION

The southern Ara OB1 association shows evidence of recent star formation that may have been triggered by a supernova event (Herbst & Havlen 1977, hereafter HH77; Arnal et al. 1987). The remarkable young stellar cluster NGC 6193 lies near the center of Ara OB1 and was first studied optically by Whiteoak (1963). A more comprehensive optical study was undertaken by HH77 who determined the foreground reddening and derived a distance of 1.32 ± 0.12 kpc. They identified the higher mass O, B, and A star cluster members,

but lower mass members have not yet been isolated. The cluster is undoubtedly young with age estimates in the range $\sim 1.5 - 3.1$ Myr (Moffat & Vogt 1973, HH77, Vázquez & Feinstein 1992).

The central part of the cluster is dominated by two luminous O-type stars HD 150135 and HD 150136, separated by only $\approx 10''$. The optical properties of these two O stars are very similar, as summarized in Table 1. Their intense ionizing radiation may be influencing star-formation in the nearby RCW 108 molecular cloud (Comerón et al. 2005).

HD 150136 is unusual in several respects. It is a massive spectroscopic binary (SB2) consisting of two O stars in a close 2.662 day orbit and has recently been classified as O3 + O6V (Niemela & Gamen 2005, hereafter NG05). The

* E-mail: skimmers@casa.colorado.edu (SLS);
szhekov@space.bas.bg (SAZ); palla@arcetri.astro.it (FP);
cassio@astro.iag.usp.br (CB)

luminosity class of the primary is not well-determined. For typical O star masses, the short 2.662 day period implies a separation of just a few stellar radii. At this close separation, wind-wind interaction is expected. In addition, HD 150136 is a strong centimeter radio source, and most of its radio flux is nonthermal (Benaglia et al. 2001). A fainter object ($V = 9.0$ mag) is visible $\approx 1.6''$ north of HD 150136 (Mason et al. 1998), and we show here that this source is also visible in the near-infrared (Sec. 3.3). By comparison, HD 150135 is slightly fainter than HD 150136 in the optical and radio. Its binary status is uncertain, but it has been classified as a possible spectroscopic binary (Garmany et al. 1980; Arnal et al. 1988).

Although NGC 6193 has been studied optically, there are no previous pointed X-ray observations. However, a bright X-ray source was detected near the position of HD 150136 (= HR 6187) in the *ROSAT* All Sky Survey (RASS). This X-ray source was identified with HD 150136 by Berghöfer et al. (1996) who obtained a luminosity in the 0.1 - 2.4 keV band of $\log L_X$ (ergs s $^{-1}$) = 33.05, making it the most luminous O star detected in the RASS. This bright source was also serendipitously detected in a 8460 s *ROSAT* PSPC exposure (image rp900554n00) at a $\approx 20'$ off-axis position with a count rate of 0.36 c s $^{-1}$, which is 40% less than reported from the RASS detection.

The presence of a luminous (and possibly variable) X-ray source in the *ROSAT* images at or near the HD 150136 position motivated us to undertake a more detailed X-ray study of the NGC 6193 cluster core with the *Chandra* X-ray Observatory (CXO). Our primary objectives were to use *Chandra's* high angular resolution to determine the precise origin of the bright X-ray emission detected by *ROSAT* and to acquire a grating spectrum capable of identifying the X-ray emission process. In addition, the sensitive (90 ksec) *Chandra* observation provides the first high-quality X-ray image of the region immediately surrounding the central O stars HD 150135 and HD 150136, allowing us to catalog the X-ray emitting population in the cluster core.

Chandra resolves the bright central X-ray source into two components corresponding to separate but unequal contributions from HD 150135 and HD 150136. Thus, the luminous X-ray source detected by *ROSAT* is found to be the superimposed contribution of the two bright O stars lying $10''$ apart. Interestingly, the long *Chandra* exposure shows that the emission of HD 150136 is slowly variable on a timescale of < 1 day. Grating X-ray spectra of HD 150135 and 150136 are similar (but not identical) and soft emission is prevalent in both stars, implying a wind shock origin. We identify 43 X-ray sources in the central $\approx 2' \times 2'$ region of the cluster. All of these have near-IR counterparts and about one-third show X-ray variability, thus being viable candidates for low-mass cluster members.

2 OBSERVATIONS

2.1 X-ray Observations

The *Chandra* observation of NGC 6193 began on 27 June 2002 at 05:20 UT and ended on 28 June at 07:12 UT, yielding an exposure live time of 90,337 seconds. The High Energy Transmission Grating (HETG) was used along with the

ACIS-S CCD detector in faint-timed telemetry mode. The nominal pointing position was (J2000.0) RA = 16h 41m 18.89s, Decl. = $-48^\circ 45' 39.3''$, which is $16.7''$ northwest of HD 150136. Further information on *Chandra* and its instruments can be found in Weisskopf et al. (2002).

Data reduction used standard data processing (“pipeline”) products and CIAO¹ processing scripts supplied by the *Chandra* X-ray Center. Data were reduced using CIAO vers. 3.0.2 and calibration data CALDB vers. 2.26. Our post-pipeline processing included steps to make use of observation-specific bad pixel files, removal of faint point sources in the regions used to extract grating spectra, destreaking of the ACIS-S4 CCD, and energy filtering to reduce the effects of low and high-energy background.

X-ray source detection was accomplished using the CIAO wavelet-based tool *wavdetect* applied to full-resolution images ($0.49'' \times 0.49''$ pixels). The images were first energy-filtered to include only photons in the [0.5 - 7.0] keV energy range, which reduces both soft and hard background emission. We ran *wavdetect* using pixel scales of 1, 2, 4, 8, and 16 pixels, and compared results for various values of the input parameter *sigthresh*, which determines the false alarm probability. Images were visually inspected for missed or spurious detections, and we found that *sigthresh* = 1.5×10^{-5} produced good results. At this value, only one spurious detection is expected in the $2.1' \times 2.1'$ (256×256 pixels) core region analyzed here (Fig. 1). The unabsorbed X-ray luminosity detection limit corresponding to a 6 count on-axis detection in the 0th order ACIS-S image is $\log L_X$ (0.5 - 7 keV) = 29.99 (ergs s $^{-1}$) at the cluster distance of 1.3 kpc. This value was determined from the Portable Interactive Mult-Mission Simulator (*PIMMS*)², assuming an isothermal Raymond-Smith plasma with a characteristic temperature $kT = 2$ keV and absorption column density $N_H = 4 \times 10^{21}$ cm $^{-2}$. These spectral parameters are typical of X-ray sources in the region (Sec. 3.2).

A total of 43 X-ray sources were detected in the core region (Table 2; Figure 1). Event lists were extracted for each source using the elliptical source regions output by *wavdetect*. The energy-filtered event lists were then used for further statistical analysis of source properties (Sec. 3.2).

Background-subtracted first order grating spectra from the medium energy gratings (MEG) and high energy gratings (HEG) were extracted for HD 150135 and HD 150136 using standard CIAO threads. The roll angle of the observation was favorable and provided adequate separation of the grating arms of HD 150135 and HD 150136 on the ACIS-S detector. However, we used a slightly narrower mask than the default value to extract the grating spectra of each star in order to avoid any possible cross-contamination. The CIAO tool *psextract* was used to extract zeroth order spectra of selected bright sources (including HD 150135 and HD 150136) along with background spectra from adjacent source-free regions.

¹ Further information on *Chandra* Interactive Analysis of Observation (CIAO) software can be found at <http://asc.harvard.edu/ciao>.

² <http://asc.harvard.edu/ciao/ahelp/pimms.html>

2.2 Near-Infrared Observations

We used the 2MASS all-sky data release³ to identify near-IR counterparts to X-ray sources in the central cluster region (Table 2). A few X-ray sources lacked 2MASS counterparts but these were identified using more sensitive near-IR images obtained with the 1.6 m Perkin-Elmer telescope at the Observatório do Pico dos Dias, Laboratório Nacional de Astrofísica, Brazil (Fig. 1). The observations were acquired on 23 July 2002 under photometric conditions ($<0.7''$ seeing) with the CamIV near-IR camera. The camera uses a 1024×1024 pixels Hawaii HgCdTe detector with $0.24''$ pixels, providing a $4' \times 4'$ field-of-view. The central region of NGC 6193 was imaged in J, H, and a narrow filter with a central wavelength $\lambda_c = 2.14 \mu\text{m}$ ($\Delta\lambda = 0.018 \mu\text{m}$). Flux calibration was achieved by observing near-infrared standard stars from Persson et al. (1998). The data were processed in the *IRAF* environment and the images were linearized, dark frame subtracted, flat-fielded, sky subtracted, and corrected for bad pixels. Final images were constructed by co-adding twelve exposures of 5 seconds each. Limiting magnitudes of the final images were $J = 19.5$, $H = 17.9$, and 14.35 at $2.14 \mu\text{m}$.

3 OBSERVATIONAL RESULTS

We present here the main observational results including images, light curves and spectra.

3.1 X-ray Image of the Central Cluster Region

Figure 1 shows the *Chandra* ACIS-S 0th order image of the central $2.1' \times 2.1'$ region of NGC 6193 centered on the optically bright O stars HD 150135 and HD 150136. Although the 0th order image covers a larger region, we restrict our analysis here to the central $2.1' \times 2.1'$ core where the *Chandra* point-spread function is sharpest (thus providing reliable source identification) and where the probability of cluster membership is high.

Chandra clearly detects both O stars. Furthermore, their emission is well-separated at *Chandra*'s high angular resolution and they are the two brightest X-ray sources in the field. *Wavdetect* detected 42 X-ray sources in this central region, and one additional source (no. 26b) was found by visual inspection. Table 2 summarizes the properties of these 43 sources along with their IR/optical identifications. Near-IR counterparts were found for all 43 X-ray sources. The two faintest sources recovered by *wavdetect* have 4 counts each (sources 8 and 16), and are classified as possible detections. However, both have near-IR counterparts and the X-ray detections are likely real. A search of the *HST* Guide Star Catalog (GSC) and USNO B1.0 catalogs revealed optical counterparts within $1''$ of the X-ray positions for 11 sources. Four of the GSC counterparts are classified as non-stellar. Included among the stellar identifications are HD 150135, HD 150136, CD-48 11069 (B0-1), CD-48 11071 (B0V), and the $V = 12.3$ mag star NGC 6193-9.

3.2 Global X-ray Properties

To obtain a quantitative measurement of variability, we computed the K-S statistic from the unbinned energy-filtered event list of each source. Further information on the K-S statistic can be found in Press et al. (1992). Fourteen sources were found to be variable (Table 2), based on the criterion that they have a probability of constant count rate $P_{\text{const}} \leq 0.05$. Two of the four OB stars are variable. These are HD 150136 ($P_{\text{const}} = 1.4 \times 10^{-8}$) and CD-48 11069 ($P_{\text{const}} = 0.02$). A moderate X-ray flare was detected in source no. 25, which has a $K = 11.4$ mag 2MASS counterpart. Since short-term (~ 1 day) variability is rarely detected in extragalactic AGNs, it is likely that most of the twelve variable sources other than HD 150136 and CD-48 11069 are stellar.

To distinguish between soft and hard sources, the mean photon energy $\langle E \rangle$ of each source (Table 2) was computed from energy-filtered event lists. Figure 2 is a histogram showing the distribution of $\langle E \rangle$. Most sources have $\langle E \rangle \approx 1.8 - 2$ keV, which is typical of coronal emission from low-mass stars. Three of the massive OB stars show a much softer photon energy distribution that is suggestive of a different X-ray emission process, probably related to shocks in their winds. These are HD 150135, HD 150136, and CD-48 11071. The latter star has spectral type B0V and was the softest source detected in the central region with $\langle E \rangle = 0.87$ keV.

An interesting exception is the early B star CD-48 11069 (source 26a), which shows a harder energy distribution $\langle E \rangle = 2.09$ keV than the other three OB stars as well as variable X-ray emission. It has been variously classified as B0-1 V or B0 IV (Reed & Beatty 1995), and radial velocity variations (Arnall et al. 1988) indicate that it is a binary. It is thus possible that the X-rays are due to a lower mass companion.

Except for the two bright O stars, only five other X-ray sources in Table 2 have >100 counts (sources 5, 14, 25, 26a, 34). Thus, spectral fitting is in most cases not practical because of insufficient counts. However, we did fit the CCD spectra of the above five sources with simple absorbed one-temperature (1T) and two-temperature (2T) *vapex* optically thin plasma models in XSPEC⁴ version 11.3.1. The fit parameters have large uncertainties but acceptable 2T fits were obtained with a cool component at $kT_1 \approx 0.1 - 0.4$ keV and a hotter component at $kT_2 \approx 1.6 - 4.5$ keV. The highest temperatures were inferred for sources 14 and 25, both of which are variable and thus likely to be magnetically-active low-mass stars. The mean (median) absorption from 2T fits of these five stars was $N_H = 5.0$ (3.5) $\times 10^{21} \text{ cm}^{-2}$, with a range of a factor of ~ 3 . This absorption is similar to that determined for the much brighter source HD 150136 (Table 3). For the B0-1 star CD-48 11069 noted above, a 2T spectral fit gives $\log N_H = 21.2$ (cm^{-2}) and a dominant hot component at $kT \approx 2.5$ keV.

³ See <http://www.ipac.caltech.edu/2mass>.

⁴ The XSPEC spectral analysis package is developed and maintained by HEASARC at NASA's Goddard Space Flight Center. See <http://heasarc.gsfc.nasa.gov/docs/xanadu/xandu.html> for additional information.

3.3 Infrared Properties

Both 2MASS and Pico dos Dias (PD) near-IR images show that the field near the cluster center ($l = 336.7^\circ$, $b = -1.57^\circ$) is crowded (Fig. 1). As a result, confusion flags are set in one or more 2MASS bands for all but 10 of the sources listed in Table 2. We thus provide here only a brief summary of the IR properties and defer a complete discussion until higher resolution images become available.

The near-IR colors of those 10 2MASS sources other than the two central O stars without confusion flags at J, H, or K are plotted in Fig. 3. We also show the colors of 4 2MASS sources with a confusion flag set only at J band (not at H or K), but with J magnitudes that were still in good agreement ($\Delta J \leq 0.2$ mag) with Pico dos Dias photometry. The 14 sources in Fig. 3 range from $K = 7.91$ (source 41 = CD -48 11071) to $K = 13.16$ (source 2), with a mean (median) $K = 11.36$ (11.49). Of the 14 sources in Fig. 3, only one shows a near-IR excess. This is source 30, which is associated with a $K = 11.19$ 2MASS counterpart and a $R = 13.5$ mag *HST* Guide Star Catalog (GSC) source. The GSC classifies the object as non-stellar.

Thus, the most reliable JHK data presently available suggest that the fraction of X-ray sources with near-IR excesses is quite low. However, higher spatial resolution near-IR photometry is needed to obtain reliable colors for closely spaced sources along with mid-IR photometry to search for cooler dust emission that might be present.

The Pico dos Dias images confirm a previously detected optical source ($V = 9.0$) located just north of HD 150136 (Mason et al. 1998). This source is clearly visible in our 2.14μ image (Fig. 4) at an offset of $\approx 1.7''$ north of HD 150136. We estimate from Pico dos Dias photometry that it is ≈ 2.4 mag fainter than HD 150136 at 2.14μ , but higher angular resolution will be needed to clearly separate the two. If this star is at the same distance as HD 150136 and has similar A_V , then it would correspond to an early B spectral type for a main sequence object. No significant X-ray emission is seen from this star, which is in the wings of the *Chandra* PSF of HD 150136.

4 THE MASSIVE O STARS HD 150135 AND HD 150136

Although the two closely-spaced O stars HD 150135 and HD 150136 have similar optical properties, their X-ray properties show differences, as discussed below.

4.1 L_X/L_{bol}

The unabsorbed X-ray luminosity (L_X) of HD 150136 is about 4 times larger than HD 150135 (Table 1). The high L_X of HD 150136 is exceptional, making it one of the brightest (if not *the* brightest) X-ray sources in the O star class. But, the HD 150136 SB2 system has a larger bolometric luminosity (L_{bol}) than HD 150135 by virtue of its earlier O3 primary and O6V companion. As a result, the L_X/L_{bol} ratios of HD 150135 and HD 150136 are nearly identical (Table 1).

The RASS study of OB stars by Berghöfer et al. (1996, 1997) established a correlation $\log L_X = 1.13 \log L_{bol} - 11.89$, with a standard deviation of 0.40 dex for stars with

$\log L_{bol}$ (ergs s $^{-1}$) > 38 . However, many OB stars were not detected in the short RASS exposures, so the mean L_X deduced from RASS data is probably too high. A similar correlation was found in *Einstein* data for O stars by Sciortino et al. (1990). As shown in Figure 5, the (L_X , L_{bol}) values for HD 150135 and HD 150136 are well within the scatter of the RASS sample, which is quite large. Thus, the (L_X , L_{bol}) values for these two O stars do not seem unusual, but the high L_X of HD 150136 is extreme for an O star.

4.2 X-ray Light Curves of HD 150135 and HD 150136

Figure 6 shows the 0th order ACIS-S light curves of both HD 150135 and HD 150136. We have considered the effects of pileup, which occurs when two or more photons are detected as a single event. Based on *PIMMS* count rate simulations using fluxes determined from the MEG1 spectra (unpiled), we estimate that 0th order pileup was $\approx 9\%$ in HD 150136 and $\approx 1\%$ in HD 150135. The low pileup level in HD 150135 is negligible and the moderate level in HD 150136 will cause the count rate to be slightly underestimated in the 0th order light curve but does not significantly affect our results. The grating data are unaffected.

No significant variability was detected in HD 150135, but HD 150136 is clearly variable. Its count rate dropped slowly by about 38% during the first 39 ksec of the observation. It then increased slowly back to levels near the initial value. The first order MEG1 light curve shows similar behavior. In addition, we extracted a light curve using a small rectangular extraction region of size 6×3 pixels ($2.9''$ EW $\times 1.5''$ NS) centered on HD 150136. This region excluded the faint optical/IR source located $1.7''$ to the north, which in any case is not clearly detected in the X-ray images. The X-ray light curve variability is still present, implying that the faint optical/IR companion is not the cause of the X-ray variability. A K-S analysis of the 0th order light curve of HD 150136 using events in the 0.5 - 5 keV range gives a probability of constant count rate $P(\text{const}) = 2.4 \times 10^{-8}$.

To further investigate the nature of the variability, we extracted energy-filtered light curves of HD 150136 in soft (0.3 - 1.5 keV) and hard (1.5 - 5 keV) bands. We found no significant variation in the hardness ratio during the light curve dip. In addition, we extracted and fitted 0th order spectra of HD 150136 during the light curve dip ($t = 24 - 48$ ksec) and after the dip ($t = 55 - 90$ ksec). Fits of these spectra with two-temperature optically thin plasma models show no significant differences in temperature or absorption. However, the total emission measure (sum of both temperature components) during the light curve dip is only 27% of that in the post-dip spectrum.

The above analysis shows that the X-ray variability in HD 150136 was linked to a drop in the emission measure and was not accompanied by any significant temperature change. This suggests that the variability may have resulted from a partial obscuration of the X-ray emitting region, as discussed further in Section 5.8.

4.3 X-ray Spectra of HD 150135 and HD 150136

Figure 7 shows the 0th order spectra of HD 150135 and HD 150136, and Figures 8 - 9 show their MEG1 spectra. We

have analyzed the 0th order and 1st order HETG spectra of both HD 150135 and HD 150136 using a variety of different models. These include discrete temperature models with one (1T), two (2T), and three (3T) temperature components, and differential emission measure (DEM) models. Spectra were rebinned to a minimum of 20 counts per bin for spectral fitting. All models included an absorption component based on Morrison & McCammon (1983) cross sections.

Discrete temperature models were based on the *bvapec* module in XSPEC, which utilizes the recent APED atomic data base and includes a *velocity* fit parameter that accounts for line broadening. The DEM was constructed using a modified version of the XSPEC Chebyshev polynomial model *c6pvmkl* (Lemen et al. 1989), as discussed below.

Overall, our most robust results are based on fits of the MEG1 spectrum of HD 150136, which provides good spectral resolution and high signal-to-noise (S/N) data. Measurements of line properties of some lines were also possible using HEG1 spectra of HD 150136 (Table 4), which provides higher spectral resolution than MEG1 at lower S/N. Because of its lower flux, our spectral fits of HD 150135 are restricted to 0th order and MEG1 spectra only.

4.3.1 X-ray Temperatures

Acceptable fits of 0th order spectra can be obtained using 2T models, as summarized in Table 3. The spectra of both HD 150135 and HD 150136 are quite soft with characteristic temperatures of $kT \approx 0.2 - 0.3$ keV. The MEG1 spectrum of HD 150135 can be acceptably fit with a 1T model having $kT = 0.3$ keV, and the 2T model (Table 3) provides only a slight improvement. In contrast, the 2T model provides a significant improvement over 1T in HD 150136. Further modest fit improvement can be obtained with a 3T model in HD 150136, which includes a third temperature component at $kT \approx 1.6$ keV, but only 9% of the total emission measure is attributed to this component.

4.3.2 Emission Measure Distribution

The DEM distribution of HD 150136 based on modeling of its MEG1 spectrum (8780 net counts) is shown in Figure 10. The DEM was determined by a global fit of the spectrum using a modified version of the *c6pvmkl* Chebyshev polynomial algorithm in XSPEC that incorporates recent APED atomic data. This global fitting strategy takes the underlying continuum into account in reconstructing the DEM. Line broadening was modeled by applying the Gaussian smoothing function *gsmooth*. Abundances were varied and converged to values close to those obtained for the 2T model (Table 3), with an inferred iron abundance $Fe = 0.32 \pm 0.09$ ($\pm 1\sigma$) solar.

As seen in Figure 10, the DEM of HD 150136 is quite soft, with a single peak near $kT \approx 0.2$ keV. The precise value of the peak is somewhat uncertain, but is very likely below 0.4 keV. We find no evidence of a second hotter emission peak but some plasma up to at least $kT \approx 1$ keV is inferred from the DEM profile.

We also attempted to reconstruct the DEM of HD 150135 using the Chebyshev polynomial method applied to its MEG1 spectrum (1100 net counts). The inferred DEM

is very similar to that of HD 150136, showing a single soft peak below $kT \approx 0.4$ keV, with almost all fits peaking at $kT \approx 0.2 - 0.3$ keV. One discernible difference is that the DEM of HD 150135 seems to be more sharply peaked, with less fractional contribution from hotter plasma at temperatures above the peak. This is consistent with the results of our discrete temperature models, which also indicate a slightly cooler plasma distribution in HD 150135.

4.3.3 Emission Line Properties

The emission line properties of HD 150135 and HD 150136 are quite similar. Both stars show broadened lines with typical broadening of $FWHM \approx 2400 - 2500$ km s⁻¹ (Table 3), no significant line centroid shifts, and little or no asymmetry. Table 4 summarizes the line properties of HD 150136, which are more reliably determined than for the fainter line emission of HD 150135. Even so, the O VII line in HD 150136 is faint and the uncertainties in its width and centroid are larger than for the other lines. A notable result is that the higher temperature S XV and Si XIV lines were detected in HD 150136 (Fig. 9), but not in HD 150135 (Fig. 8). MEG1 spectral simulations show that if the temperature structure of HD 150135 were the same as that of HD 150136, these two lines should have been detected in HD 150135 in spite of its lower count rate. We thus conclude that the plasma of HD 150136 is slightly hotter than that of HD 150135, as already suggested by discrete temperature models.

4.3.4 He-like Triplets

Observed fluxes were measured for the resonance (*r*), intercombination (*i*), and forbidden (*f*) line components in He-like triplets of HD 150136 using 1st order grating spectra. The flux ratios $R = f/i$ and $G = (f + i)/r$ are given in Table 4, and the Si XIII triplet is shown in Figure 11. To measure the fluxes of individual components, He-like triplets were fitted with 3-component Gaussian models plus a constant term to account for the underlying continuum. To reduce the number of free parameters in the fit, the ratios of the wavelengths of the *r*, *f*, and *i* lines were held fixed during the fitting process at their laboratory values. In addition, line broadening was taken into account. The line width was allowed to vary during the fit, but the widths of all three components were constrained to be equal.

The *G* ratio is sensitive to temperature and the *R* ratio is sensitive to the electron density (*n*) and stellar UV radiation field (Gabriel & Jordan 1969). If ϕ is the photoexcitation rate from the $1s2s\ ^3S_1$ *f* level to the $1s2p\ ^3P_1$ *i* level, then $R = R_0/[1 + (\phi/\phi_c) + (n/n_c)]$, where ϕ_c and n_c are the critical photoexcitation rate and critical density (Blumenthal, Drake, & Tucker 1972; Porquet et al. 2001). If photoexcitation and collisions are both negligible, then $R \rightarrow R_0$, where R_0 is referred to as the low-density limit. Either high electron densities or strong photoexcitation can lead to $R < R_0$.

We obtain $R < R_0$ for all He-like triplets measured in HD 150136, with S XV being a possible exception (Table 4). As discussed above, the suppressed *R* values could be due to high electron densities or intense UV radiation (or both). However, it is unlikely that the suppression can be explained

by high densities. As an example, consider Ne IX λ 13.447 Å, for which $n_e \sim 10^{11} \text{ cm}^{-3}$ (Porquet & Dubau 2000). Assuming a spherically symmetric homogeneous solar-abundance wind, mass loss parameters as in Table 5, and a conventional wind velocity profile $v(r) = v_\infty[1 - (R_*/r)]^\beta$ with $\beta = 1$, densities $n \gtrsim n_e$ are anticipated only at radii $r \lesssim 1.2 R_*$ for an O3V primary, and the corresponding radius for O3I is about 30% larger. However, it is clear that the Ne IX line cannot originate at $r \lesssim 1.2 R_*$ because the radius of optical depth unity for O3V at the Ne IX line energy 0.92 keV is $R_{\tau=1}(0.92 \text{ keV}) \approx 5.5 R_*$, and about five times larger for O3I. To estimate $R_{\tau=1}$, we have used solar abundance cross-sections (Balucinska-Church & McCammon 1992; Anders & Grevesse 1989) along with the O3 stellar parameters in Table 5. Thus, the optical depth constraint places the region of line formation for Ne IX outside the radius at which density suppression would be important. We emphasize that this conclusion rests on the assumption of a spherical homogeneous wind. If the wind is clumped (Sec. 5.4), then $R_{\tau=1}$ is reduced and line formation could occur at smaller radii than inferred above.

It is more likely that the low R values result from photoexcitation by the strong UV field of the O3 + O6V system. The distance at which UV effects become significant is measured by the critical radius R_c , where the photoexcitation rate from the upper level of the f transition equals the spontaneous decay rate from that same level. Triplets forming at $r < R_c$ will have UV-suppressed R ratios. Values of R_c for O3V are given in Table 4 for each He-like triplet.

Figure 12 shows $R_{\tau=1}$ and R_c values for He-like triplets in HD 150136. In general, UV-suppressed triplets could form at radii $R_{\tau=1} < r < R_c$, as shown graphically by the solid lines in Figure 12. But, in HD 150136 the R ratios are strongly suppressed and it is more likely that $r \ll R_c$. In any case, it is apparent from Figure 12 that triplets with higher maximum line power temperatures such as S XV and Si XIII are formed closer to the star than lower temperature lines such as Ne IX and O VII.

4.3.5 Abundances

The MEG1 spectrum of HD 150136 is of sufficient quality to derive basic abundance information (Table 4). The strongest result is that Fe is underabundant with respect to the solar photospheric value by a factor of $\approx 4 - 5$, and quite likely Ne as well. The Fe underabundance is also clearly seen in the MEG1 spectrum of HD 150135. Low Fe abundances have also been reported for other massive young stars such as Trapezium OB stars (Schulz et al. 2003). For HD 150136, O and S abundances have the largest uncertainties.

5 DISCUSSION

We summarize here the stellar properties of HD 150135 and HD 150136 that are relevant to the X-ray analysis, and discuss the implications of the new *Chandra* results for our understanding of the X-ray emission in massive young stars.

5.1 The Short-Period Binary System HD 150136

The orbital period of the O3 + O6V system is 2.662 ± 0.002 days, the orbit is nearly circular ($e = 0.03 \pm 0.02$), and the inclination is probably low since optical eclipses have not been seen (NG05). The luminosity class of the O3 primary is not well-determined, and we consider both O3I and O3V. Adopting the O star parameters listed in Table 5, the orbital semi-major axis from Kepler's 3rd law is $a = 0.165 \text{ AU}$ for a O3V primary and $a = 0.173 \text{ AU}$ for O3I. In units of O3 star radii, this separation equates to only 2.1 - 2.7 R_* . Thus, this remarkable O + O system is nearly in contact. As a result of the close separation, interaction of the O3 and O6V winds seems unavoidable and may lead to X-ray emission from a colliding wind (CW) shock, as discussed further below.

5.2 Is HD 150135 a Binary?

The binary status of HD 150136 is firmly established (NG05) but the evidence for binarity in HD 150135 is not as conclusive. Garmany et al. (1980) classified it as a possible SB1 based on large radial velocity differences in three spectra. Arnal et al. (1988) obtained 17 radial velocity measurements over 10 days and classified it as a possible SB2.

The radio continuum emission of HD 150135 (and HD 150136) is unusually strong for a star of its spectral type, giving further reason to suspect binarity. The flux density of HD 150135 increases with frequency with a 3.5 cm value $S_{3.5\text{cm}} = 0.28 \pm 0.03 \text{ mJy}$ (Benaglia et al. 2001). If this flux is attributed entirely to free-free wind emission, then the inferred mass loss rate at $d = 1.3 \text{ kpc}$ is $\log \dot{M} = -5.4 M_\odot \text{ yr}^{-1}$. This value is about an order of magnitude larger than determined for other O6.5V stars (Garmany et al. 1981; Lamers & Leitherer 1993). It is thus possible that some of the radio flux is nonthermal, as is the case for HD 150136.

The above results point toward binarity in HD 150135, but nothing is known about the putative companion. The *Chandra* data do not show any telltale hints of binarity such as variability or hard X-ray emission that might arise in a colliding wind shock. Its L_X/L_{bol} ratio is high, but within the scatter of the RASS sample and nearly on the regression line for O stars determined by Sciortino et al. (1990) (Fig. 5).

5.3 Wind Parameters

An estimate of the terminal wind speed is available for HD 150136 (Prinja et al. 1990) but not for HD 150135. Both stars are radio continuum sources (Benaglia et al. 2001), but HD 150136 contains a nonthermal contribution, as may HD 150135 (Sec. 5.2). Thus, estimates of the mass loss rates based on radio continuum fluxes are likely to be incorrect. In the absence of reliable observational data, we have adopted the mass loss parameters given in Table 5, which are representative of O3 and O6V stars in general.

5.4 Line Properties and Clumped Winds

The line widths of HD 150136 in Table 4 reveal interesting trends. The widths of all lines are similar, with a mean $\text{FWHM} = 2100 \text{ km s}^{-1}$. Then, $\text{HWHM} = 1050 \text{ km s}^{-1}$,

or $\overline{\text{HWHM}} \approx v_\infty/3$ (Table 5). Thus, the lines are broadened, but not nearly as broad as might be expected if they were formed in the outer wind where the wind is at terminal speed. A similar situation exists for HD 150135, whose mean line width as determined from MEG1 spectra is nearly identical to that found in HD 150136. Recent *Chandra* grating observations of other young O stars such as σ Ori AB (O9.5V) also show very moderate line broadening with $\text{HWHM} \approx v_\infty/4$ (Skinner et al. 2004).

If one attributes the broadening to X-ray line formation in an outflowing stellar wind (Owocki & Cohen 2001), then a $\beta = 1$ wind acceleration profile (Sec. 4.3.4) gives $v(r) = \overline{\text{HWHM}} = 1050 \text{ km s}^{-1}$ at $r \approx 1.5 R_*$. Comparing against Figure 12, it is apparent that higher temperature lines could form at such small radii but cooler lines such as Ne IX and O VII are expected to form further out because of their larger $R_{\tau=1}$ values. Thus, there is an apparent contradiction. Moderately broadened lines suggest that the lines are formed in the wind acceleration zone close to the star, but optical depth calculations require larger formation radii for cooler lines, where the wind should be at or near its terminal speed.

The above inconsistency may be due to our imprecise knowledge of the mass loss parameters, wind opacities, and wind structure. The wind acceleration profile is not empirically determined, and the mass-loss rate, which enters into the optical depth unity calculation, is poorly-known. Lastly, the assumption of a spherical homogeneous wind may be overly simplistic. It has been suggested that O star winds may be clumped and that clumping could account for discrepancies in O star mass loss rates determined by different methods (Fullerton et al. 2004; Repolust et al. 2004). If the wind is clumped then the optical depth at a given line energy would be reduced and line photons could escape from smaller radii than indicated by Figure 12, resulting in less broadening than expected for a homogeneous wind (Owocki & Cohen 2001).

5.5 Colliding Winds in HD 150136

The close separation in the HD 150136 O3 + O6 system virtually assures wind-wind interaction. We would thus like to know if some or all of its prodigious X-ray emission could be due a colliding wind shock, which is expected to form in the harsh radiation environment between the two O stars. There are indeed signs that the X-ray emission of HD 150136 may be influenced by binarity. As we have seen, its X-ray emission is slightly hotter and a factor of four more luminous than its optical twin HD 150135. In addition, its strong non-thermal radio emission may signal shock processes. Because of the close binary separation, the radiation-hydrodynamics problem is coupled and is challenging to model numerically.

5.5.1 Non-adiabatic Colliding Wind Shocks

The temperature of shocked gas at the shock interface in an *adiabatic* colliding wind shock is proportional to the square of the pre-shock wind velocity component normal to the interface (eq. [1]. of Luo et al 1990). For wind speeds typical of O stars (Table 5), X-ray temperatures of several keV are expected and have been observed in such wide systems as the 7.9 year WR + O binary WR 140 (Zhekov & Skinner 2000).

In contrast, we detect very little hot plasma above ~ 1 keV in HD 150136 (Fig. 10). Because of its closer separation, the winds will not have reached terminal speeds before colliding and radiative cooling will be important. As a result, colliding wind shock emission could be present at lower temperatures than predicted in the adiabatic case.

The parameter used to determine whether a colliding wind shock is adiabatic or non-adiabatic is the ratio $\chi = t_{\text{cool}}/t_{\text{esc}}$, where t_{cool} is the characteristic cooling time for shock-heated gas and t_{esc} is the escape time for gas to flow out of the intershock region. If $\chi \gtrsim 1$ then the system is adiabatic while $\chi \ll 1$ implies the system is non-adiabatic and radiative cooling is important. Adopting O3V wind parameters for HD 150136 (Table 5) and a $\beta = 1$ velocity law, we obtain $\chi(\text{O3V}) = 0.2$ (eq. [8] of Stevens et al. 1992, hereafter SBP92). Thus, HD 150136 is a non-adiabatic system.

5.5.2 Colliding Wind Simulations

The numerical hydrodynamic simulation of colliding winds in closely-spaced non-adiabatic systems is complex. Cooling processes and wind acceleration must be taken into account. Also, radiative braking may be important, whereby the radiation of one O star slows the wind of its companion (Owocki & Gayley 1995). The presence of a mathematical singularity at the stagnation point on the line-of-centers has hindered the development of rigorous numerical hydrodynamic models, as discussed by Myasnikov et al. (1998).

Because of the above complexities, we have only developed simplified hydrodynamic CW simulations of HD 150136 to date. We assume O3V + O6V wind parameters, a $\beta = 1$ velocity law, and the orbit solution of NG05. The simulations invoke wind momentum balance and the shock surfaces are assumed to follow the contact discontinuity (Luo et al. 1990; SBP92), as expected for efficient cooling. Cooling from an optically thin plasma was included using the approach of Myasnikov et al. (1998), as well as cooling from Comptonization (Myasnikov & Zhekov 1993).

The simulations indicate that a CW shock model alone cannot account for all of the observed X-ray properties of HD 150136. Specifically, the CW model underestimates N_{H} by about an order of magnitude, and also places a larger fraction of the emission measure in hot plasma ($kT \gtrsim 1 \text{ keV}$) than expected from the observationally determined DEM (Fig. 10).

The above results indicate that if CW shock emission is present, then it is supplemented by an additional cool component, which would most likely originate in the O stars themselves. X-ray emission from cool plasma in the shocked line-driven winds of the individual O stars is indeed expected (Lucy & White 1980; Lucy 1982). To test this idea, we attempted to fit the MEG1 spectrum of HD 150136 using a hybrid 1T + CW model, where the isothermal 1T thin plasma component accounts for cool shocked plasma in the O-star winds.

This hybrid model provides a much better fit to the spectrum than does the pure CW model, resulting in a 37% decrease in reduced χ^2 ($\chi^2/\text{dof} = 213/377$). The hybrid model satisfactorily reproduces the overall spectral shape, observed flux, and N_{H} , and converges to abundances that are very close to those obtained in discrete 2T fits (Table 3). The 1T component in the hybrid model converges to kT

≈ 0.3 keV, consistent with expectations from cool shocked plasma in the O star winds. Roughly half of the observed flux could come from the O stars themselves. However, we note that our *a priori* estimate of the emission measure from the CW shock is a few times larger than needed to accurately reproduce the MEG1 spectrum. Several factors could account for this including inaccuracies in the orbit solution or the assumed mass loss rates, or oversimplifications in the CW hydrodynamic model.

The hybrid 1T + CW model offers a potential explanation of the X-ray properties of HD 150136. But, additional refinements in the CW model as well as a more accurate orbit solution and determination of the luminosity class of the primary will probably be needed to determine if the hybrid model can be fully reconciled with the data. Further refinements in the CW shock model will include radiative braking and accounting for the effects of orbital motion on the emission line properties.

5.6 Magnetically Confined Winds

X-ray grating spectra recently obtained for several massive young stars have sparked renewed interest in the possibility that their winds might in some cases be magnetically confined. This has been the result of the detection of narrow emission lines and hot plasma ($kT \gtrsim 2$ keV) in young objects such as the O star θ^1 Ori C (Schulz et al. 2000) and the unusual B star τ Sco (Cohen et al. 2003). Narrow unshifted lines and hot plasma are usually associated with magnetically trapped plasma and are difficult to explain in the context of classical (non-magnetic) wind shock theory.

The influence of a dipole magnetic field on the outflowing wind of a luminous hot star has been discussed by ud-Doula & Owocki (2002). The degree to which the wind is confined by the field is measured by the confinement parameter $\eta = (0.4 B_{100}^2 R_{12}^2) / (\dot{M}_{-6} v_8)$ where B_{100} is the equatorial magnetic field surface strength in units of 100 G, R_{12} is the stellar radius in units of 10^{12} cm, \dot{M}_{-6} is the mass loss rate in units of $10^{-6} M_{\odot} \text{ yr}^{-1}$, and v_8 is the wind speed in units of 10^8 cm s^{-1} . If $\eta > 1$ (strong confinement) then the wind is confined by the B field and is channeled toward the magnetic equator, where the wind components from each hemisphere collide to form a magnetically confined wind shock (MCWS), accompanied by hard X-ray emission (Babel & Montmerle 1997). If $\eta < 1$ (weak confinement), the field is opened by the dominant wind and no hard X-rays are predicted.

Since HD 150135 and HD 150136 are massive young stars, we ask if the above model could be relevant to their X-ray emission. It is clear that we do not detect the hot ($kT \gtrsim 2$ keV) plasma or the very narrow lines that the MCWS model attempts to explain in other stars. Thus, there is no compelling reason to invoke this model in the present case, at least in the strong confinement limit where $\eta > 1$. If this model is relevant at all for the O stars studied here, it must be in the weak confinement regime where $\eta < 1$. For critical confinement ($\eta = 1$) the mass loss parameters in Table 5 (O3V) give $B_{crit} \approx 400$ G. Thus, surface fields no larger than a few hundred Gauss would be expected for HD 150136. Similarly, the magnetically confined wind model of Usov & Melrose (1992) gives a surface field estimate of ≈ 140 G in the weak-field approximation.

5.7 Magnetic Fields and Early Evolution

Previous studies of NGC 6193 gave age estimates of $\sim 1.5 - 3.1$ Myr (Moffat & Vogt 1973; HH77; Vázquez & Feinstein 1992). We can now compare these with estimates of the ages of the central O stars based on updated evolutionary models. For this purpose, we use the grids of Schaller et al. (1992). Because of the complications of determining the photometric and spectroscopic properties of the two O stars in the HD 150136 SB2 system, we consider HD 150135 as a more reliable age indicator (but keeping in mind that it may also be a binary). Its absolute magnitude is $M_v = -5.33$ (HH77). The O star parameters of Vacca et al. (1996) for luminosity class V then give $\log T_{eff} = 4.66$, $\log (L/L_{\odot}) = 5.727$, and an evolutionary mass $M_{evol} = 56.6 M_{\odot}$. Using these stellar parameters, the Schaller et al. tracks for metallicity $Z = 0.020$ and $60 M_{\odot}$ give an age of ~ 1 Myr. A similar age is expected for HD 150136 because of its close association with HD 150135.

The age of ~ 1 Myr deduced for HD 150135 and, by association, for HD 150136 is a few times larger than the estimated age of ~ 0.3 Myr for Trapezium OB stars, which may still be on the zero-age main sequence (Schulz et al. 2003). It is notable that several high-mass stars in the Trapezium such as θ^1 Ori C show signs of magnetic behavior such as hot plasma, very narrow emission lines, and periodic X-ray variability (Schulz et al. 2003, Feigelson et al. 2002, Gagné et al. 1997). In contrast, we do not detect obvious X-ray magnetic signatures in HD 150135 or HD 150136, although periodic X-ray variability in the latter is not yet ruled out due to limited time monitoring. In the absence of any recognizable magnetic X-ray behavior, it may well be that any primordial magnetic fields that were initially present in HD 150135 or HD 150136 have already decayed to low levels. If that is the case, then the estimated age of ~ 1 Myr suggests that the timescale for magnetic decay is quite short, and the possibilities for studying magnetic behavior in O stars may be limited to the very youngest objects that are still on the zero-age main sequence.

5.8 X-ray Variability in O Stars

As discussed in Section 4.2, HD 150136 shows slow X-ray variability in the form of a dip in its light curve spanning at least ~ 30 ksec (Fig. 6). The variability was detected at high statistical significance in both the 0th order and MEG 1st order light curves. Simultaneous light curves of HD 150135 lying $10''$ away on the same detector show no significant variability. These factors leave little doubt that the X-ray variability of HD 150136 is real.

X-ray variability in O stars has been known since early observations with the *Einstein* observatory, but its origin is not yet understood and more than one mechanism may be involved. Collura et al. (1989) detected significant variability in three of twelve OB stars observed with the *Einstein* IPC. The variability occurred on timescales of a few days with typical variability amplitudes of $\approx 17\% - 34\%$. We find a similar variability amplitude for HD 150136, whose count rate fluctuated $+16\%/-22\%$ about the mean. Lower amplitude variability at the 6% level was reported from *ROSAT* observations of the O4 supergiant ζ Puppis (Berghöfer et al. 1996b). Variability was also detected in three O stars in the

Orion Nebula Cluster (ONC) observed by *Chandra* (Feigelson et al. 2002). These were θ^1 Ori C (O6pe), θ^1 Ori A (O7), and θ^2 Ori A (O9.5Vpe). The latter star underwent a rapid flare.

There are several possibilities for explaining X-ray variability in O stars. These can be broadly categorized as (i) magnetic processes, (ii) changes in the wind (e.g. density variations or time-variable shock structures), and (iii) dynamical effects. The latter category is quite broad and is meant to include phenomena such as (partial) eclipses of the X-ray emitting region by a companion, changes in X-ray absorption caused by the wind or atmosphere of a companion moving into the line of sight, changes in orbital separation in CW systems, and rotational modulation of X-ray emitting structures on or near the star.

Intrinsic variability associated with magnetic processes is usually accompanied by high-temperature plasma ($kT \gg 1$ keV) and/or rapid magnetic reconnection flares. Dramatic temperature changes can occur on timescales of minutes to hours in magnetic flares. We do not detect high-temperature plasma in HD 150136, nor do we see any significant temperature changes or rapid impulsive flares. Thus, the existing data for HD 150136 do not obviously point toward a magnetic origin for the slow variability. But the temporal coverage is so far quite limited and spans only 39% of the 2.662 day orbit. Observations spanning a longer time period are needed.

Changes in the wind density at the base of the wind were cited as a possible explanation of the X-ray variability detected by *ROSAT* in the O4 supergiant ζ Pup (Berghöfer et al. 1996b). However, the mechanism that would drive such density perturbations is not known. Along similar lines, Feldmeier et al. (1997) have attributed the X-ray variability in O stars to the collision of dense shells of gas in their winds. This model predicts short X-ray variability timescales of ~ 500 s. This is much shorter than the variability timescale of several hours observed in HD 150136, but one might argue that variability timescales of \sim hours could result from successive collisions of dense shells (Fig. 19 of Feldmeier et al. 1997). Apart from the timescale question, the high X-ray luminosity of HD 150136 may be even more problematic for the shell-collision picture. Typical X-ray luminosities predicted by shell-collision simulations are $\log L_X \approx 32.3$ (ergs s^{-1}), with model-dependent standard deviations of ± 0.4 to ± 0.6 . This predicted L_X is about an order of magnitude less than determined for HD 150136, even after halving the total L_X (Table 1) to account for two stars in the system. It thus remains to be shown that the shell-collision mechanism can account for the very high X-ray luminosity and slow variability of HD 150136.

Finally, we consider dynamic effects. These are indeed relevant because HD 150136 is known to be a 2.662 d binary. During our observation, the orbital phase of HD 150136 ranged from $\phi = 0.1 - 0.5$, where the primary is in front at $\phi = 0.5$ (NG05). The dip in the light curve is centered near $\phi \approx 0.27$ (Fig. 6). At this phase, the system is near quadrature, with the O3 primary approaching the observer and the O6 secondary receding.

In colliding wind systems, X-ray variability can be induced by orbital motion. The intrinsic luminosity of a CW shock is predicted to scale inversely as the distance between the two components (SBP92), but the orbit of HD 150136 is

nearly circular ($e = 0.03$; NG05) so no significant variability due to changes in orbital separation is expected. Also, a reduction in the observed X-ray flux can occur in colliding wind binaries from increased wind absorption as the primary moves in front of the secondary. Again, this does not explain the dip in the HD 150136 light curve, which occurs near quadrature and not when the primary is in front. To explain the light curve dip at quadrature in terms of colliding wind geometry, one would have to postulate that some of the CW shock emission on the downstream side of the secondary is being shadowed by the secondary itself.

A possible clue to the origin of the X-ray variability comes from the optical spectra of NG05. They note that the radial velocity changes in the He I absorption lines of HD 150136 do not follow the orbital motion of either the primary or secondary. Furthermore, they detect an *additional* faint absorption component redward of the He I absorption lines when the secondary of the SB2 system has maximum positive radial velocity, which occurs at phase $\phi = 0.25$. This may signal the presence of a third massive star in the system. We emphasize that this putative third component in the spectroscopic system is *not* the faint star lying $1.7''$ to the north (Fig. 4), whose position is well-known from optical studies (Mason et al. 1998).

It may not be a coincidence that the appearance of the additional optical absorption component occurs at $\phi = 0.25$, where the dip in the X-ray spectrum is also observed (Fig. 6). If the additional absorption feature is due to a massive third component moving in front at $\phi = 0.25$, then this third star (or its wind) could be partially occulting the X-ray emitting region. Such an occultation would be consistent with the observed decline in emission measure, without an accompanying temperature change. However, a physical connection between the X-ray variability and the putative third star remains quite speculative. It might be argued that a physical connection is unlikely, since it seems to require that the orbit of the third star be synchronous with that of the SB2 system. Clearly, further observational work is needed to determine if there is a connection. This would include confirmation of the existence of the putative third star, determination of its spectral type and orbit, and extended time monitoring to search for periodicity in the X-ray light curve.

A final possibility worth mentioning is that the X-ray variability of HD 150136 might be due to rotational modulation of an X-ray emitting structure that is close to the star. In that case, the observed variability could result from self-occultation, rather than from occultation by a putative third star in the system. Rotational self-occultation has been invoked to explain the X-ray variability of θ^1 Ori C (Gagné et al. 2005). Its variability is caused by a change in emission measure without an accompanying temperature change, which is qualitatively similar to the behavior that we see in HD 150136. The key question that remains is whether the X-ray variability in HD 150136 is periodic and if so, what is the period?

6 SUMMARY

We have presented results of the first X-ray observation targeted at the center of the young stellar cluster NGC 6193 in the Ara OB1 association, supplemented by ground-based

near-IR images. The main results of this study are summarized as follows:

(i) *Chandra* detected 43 X-ray sources in a $\approx 2' \times 2'$ region centered on the O stars HD 150135 and HD 150136. The strong X-ray emission previously seen by *ROSAT* is now attributed to separate but unequal contributions from HD 150135 and HD 150136. The X-ray luminosity of HD 150136 is exceptional ($\log L_X = 33.39$ ergs s $^{-1}$) making it one of the most X-ray luminous O stars known.

(ii) All 43 X-ray sources in the central cluster region have near-IR counterparts, but only eleven have optical identifications. One of these, the early B star CD-48 11069, shows an unusually hard photon energy distribution, raising the possibility that its X-ray emission arises in a low-mass companion. The population of fainter X-ray sources surrounding the central O stars is characterized by moderately hard emission with mean photon energies $\langle E \rangle \approx 2$ keV and about one-third are variable. The variable objects are promising candidates for low-mass pre-main-sequence stars in the cluster, but membership remains to be determined. The available JHK photometry suggest that the fraction of X-ray sources in the central cluster region with near-IR excesses is low. Further searches for excesses in the mid-IR are needed.

(iii) High-quality X-ray grating spectra of HD 150135 and HD 150136 show similar, but not identical, spectral properties. In both stars, the emission is dominated by cool plasma (kT ≈ 0.3 keV). The emission lines show no significant centroid shifts and are moderately broadened to $\text{HWHM} \approx v_\infty/3$. Broadened lines and cool plasma implicate wind shock emission as the origin of the X-rays. Forbidden lines in He-like triplets are strongly suppressed by the HD 150136 UV radiation field, implying that some high-temperature lines such as S XV form in the wind-acceleration zone within a few radii of the star. Optical depth and line broadening considerations hint that the wind may be clumped.

(iv) The exceptionally high X-ray luminosity of HD 150136, along with nonthermal radio emission, suggest that colliding wind shocks may be present in this closely-spaced O3 + O6V binary. However, simplified numerical simulations show that a CW shock alone cannot account for all of the observed X-ray properties. If CW emission is present, then it is supplemented by another cool X-ray component, which likely originates in the shocked winds of the individual O stars.

(v) An unexpected result is that the X-ray emission of HD 150136 is slowly variable on a timescale of $\lesssim 1$ day. The variability is due to a change in the emission measure, with little or no change in X-ray temperature, suggesting that it is an occultation effect. The mechanism responsible for the occultation is not yet known, but self-occultation due to stellar rotation or partial occultation of the X-ray emitting region by a putative third star in the HD 150136 system are possibilities. Further observational work, including long-term X-ray monitoring, will be needed to identify the origin of the X-ray variability.

ACKNOWLEDGMENTS

This research was supported by NASA/SAO grant GO2-3025X. This publication makes use of data products from the Two Micron All Sky Survey (2MASS), which is a joint project of the Univ. of Massachusetts and the Infrared Processing and Analysis Center / California Institute of Technology, funded by the National Aeronautics and Space Administration and the National Science Foundation. The results presented here are partially based on observations made at Observatório do Pico dos Dias/LNA. SZ and FP acknowledge partial financial support from the Bulgarian Academy of Sciences - Consiglio Nazionale delle Ricerche bilateral cooperation program. CB thanks FAPESP and Inst. do Milênio for financial support.

REFERENCES

- Anders, E., Grevesse, N., 1989, *Geochim. Cosmochim. Acta*, 53, 197
- Arnal, E.M., Cersosimo, J.C., May, J., Bronfman, L., 1987, *A&A*, 174, 78
- Arnal, M., Morrell, N., Garcia, B., Levato, H., 1988, *PASP*, 100, 1076
- Babel, J., Montmerle, T., 1997, *ApJ*, 485, L29
- Balucinska-Church, M., McCammon, D., 1992, *ApJ*, 400, 699
- Benaglia, P., Cappa, C.E., Koribalski, B.S., 2001, *A&A*, 372, 952
- Berghöfer, T.W., Baade, D., Schmitt, J.H.M.M., Kudritzki, R.-P., Puls, J., Hillier, D.J., Pauldrach, A.W.A., 1996b, *A&A*, 306, 899
- Berghöfer, T.W., Schmitt, J.H.M.M., Cassinelli, J.P., 1996, *A&AS*, 118, 481
- Berghöfer, T.W., Schmitt, J.H.M.M., Danner, R., Cassinelli, J.P., 1997, *A&A*, 322, 167
- Bessell, M.S., Brett, J.M., 1988, *PASP*, 100, 1134
- Blumenthal, G.R., Drake, G.W., Tucker, W.H., 1972, *ApJ*, 172, 205
- Cohen, D.H. et al., 2003, *ApJ*, 586, 495
- Collura, A. et al., 1989, *ApJ*, 338, 296
- Comerón, F., Schneider, N., Russeil, D., 2005, *A&A*, in press
- Feigelson, E.D. et al., 2002, *ApJ*, 574, 258
- Feldmeier, A., Puls, J., & Pauldrach, A.W.A., *A&A*, 322, 878
- Fullerton, A.W., Massa, D.L., Prinja, R.K., 2004, *BAAS*, 36 (No. 5), 1425
- Gabriel, A.H., Jordan, C., 1969, *MNRAS*, 145, 241
- Gagné, M., Caillault, J.-P., Stauffer, J.R., Linsky, J.L., 1997, *ApJ*, 478, L87
- Gagné, M. et al., 2005, *ApJ*, in press.
- Garmany, C.D., Conti, P.S., Massey, P., 1980, *ApJ*, 242, 1063
- Garmany, C.D., Olson, G.L., Conti, P.S., Van Steenberg, M.E., 1981, *ApJ*, 250, 660
- Gorenstein, P., 1975, *ApJ*, 198, 95
- Herbst, W., Havlen, R.J., 1977, *A&AS*, 30, 279 (HH77)
- Hillenbrand, L.A., 1997, *AJ*, 113, 1733
- Kahn, S.M. et al., 2001, *A&A*, 365, L312
- Lamers, H.J.G.L.M., Leitherer, C., 1993, *ApJ*, 412, 771

- Lemen, J.R., Mewe, R., Schrijver, C.J., Fludra, A., 1989, ApJ, 341, 484
- Lucy, L.B., 1982, ApJ, 255, 286
- Lucy, L.B., White, R.L., 1980, ApJ, 241, 300
- Luo, D., McCray, R., MacLow, M.-M., 1990, ApJ, 362, 267
- Mason, B.D. et al., 1998, AJ, 115, 821
- Moffat, A.F.J., Vogt, N., 1973, A&AS, 10, 135
- Morrison, R., McCammon, D., 1983, ApJ, 270, 119
- Myasnikov, A.V., Zhekov, S.A., 1993, MNRAS, 260, 221
- Myasnikov, A.V., Zhekov, S.A., Belov, N.A., 1998, MNRAS, 298, 1021
- Niemela, V.S., Gamen, R.C., 2005, MNRAS, 356, 974 (NG05)
- Owocki, S.P. & Cohen, D.H., 2001, ApJ, 559, 1108
- Owocki, S.P. & Gayley, K.G., 1995, ApJ, 454, L145
- Persson, S.E., Murphy, D.C., Krzeminski, W., Roth, M., Rieke, M.J., 1998, AJ, 116, 2475
- Porquet, D., Dubau, J., 2000, A&AS, 143, 495
- Porquet, D., Mewe, R., Dubau, J., Raassen, A.J.J., Kaastra, J.S., 2001, A&A, 376, 1113
- Press, W.H., Teukolsky, S.A., Vetterling, W.T., Flannery, B.P., 1992, Numerical Recipes in Fortran: The Art of Scientific Computing (2nd ed., New York: Cambridge Univ. Press)
- Prinja, R.K., Barlow, M.J., Howarth, I.D., 1990, ApJ, 361, 607
- Reed, B.C., Beatty, A.E., 1995, ApJS, 97, 189
- Repolust, T., Puls, J., & Herrero, A., 2004, A&A, 415, 349
- Rieke, G.H., Lebofsky, M.J., 1985, ApJ, 288, 618
- Schulz, N.S., Canizares, C.R., Huenemoerder, D., Lee, J.C., 2000, ApJ, 545, L135
- Schulz, N.S., Canizares, C.R., Huenemoerder, D., Tibbets, K., 2003, ApJ, 595, 365
- Schaller, G., Schaerer, D., Meynet, G., Maeder, A., 1992, A&AS, 96, 269
- Sciortino, S. et al., 1990, ApJ, 361, 621
- Skinner, S., Cohen, D., Gagné, M., Owocki, S., Townsend, R., 2004, BAAS, 36 (No. 5), 1520
- Stevens, I.R., Blondin, J.M., Pollock, A.M.T., 1992, ApJ, 386, 265 (SBP92)
- ud-Doula, A., Owocki, S.P., 2002, ApJ, 576, 413
- Usov, V.V. & Melrose, D.B., 1992, ApJ, 395, 575
- Vacca, W.D., Garmany, C.D., Shull, J.M., 1996, ApJ, 460, 914
- Vázquez, R.A., Feinstein, A., 1992, A&AS, 92, 863
- Weisskopf, M.C., Brinkman, B., Canizares, C., Garmire, G., Murray, S., Van Speybroeck, L., 2002, PASP, 114, 1
- Whiteoak, J.B., 1963, MNRAS, 125, 205
- Zhekov, S.A., Skinner, S.L., 2000, ApJ, 538, 808

Table 1. Stellar Properties

Property	HD 150135	HD 150136	Reference ^a
Spectral type	O6.5V + ?	O3 + O6V	(1),(3)
Binary	possible (SB1)	yes (SB2)	(2),(4)
P_{orb} (d)	...	2.662	(3)
V (mag)	6.89	5.62	(1)
E(B−V)	0.49	0.48	(1)
A_V (mag)	1.7	1.7	(1)
M_V (mag)	−5.33	−6.56	(1)
v_∞ (km s ^{−1})	[2455] ^b	3160	(5)
Distance (kpc) ^c	1.32 ± 0.12	1.32 ± 0.12	(1)
F_X (10^{-12} ergs cm ^{−2} s ^{−1}) ^d	0.5 (3.0)	3.3 (12.1)	(6)
log L_X (ergs s ^{−1}) ^e	32.78	33.39	(6)
log (L_X/L_{bol}) ^f	−6.3	−6.4	(6)

^aRefs.: (1) Herbst & Havlen (1977) (2) Arnal et al. (1988)

(3) Niemela & Gamen (2005) (4) Garmany, Conti, & Massey (1980)

(5) Prinja et al. (1990) (6) this work

^b Typical value for O6.5V (Prinja et al. 1990)^c To association (HH77)^d X-ray flux (F_X) is the absorbed value in the 0.5 - 6 keV band followed in parentheses by the unabsorbed value. Fluxes are from best-fit models of *Chandra* spectra using an absorption column density $N_H = 4 \times 10^{21}$ cm^{−2}.^eX-ray luminosity (L_X) is the unabsorbed value in the 0.5 - 6 keV band at a distance of 1.3 kpc.^f L_{bol} is from Vacca et al. (1996). The undetermined luminosity class of the primary in the HD 150136 system (O3 + O6V) leads to an uncertainty of ± 0.1 dex in L_{bol} .

Table 2. X-Ray Sources in the NGC 6193 Core Region

No.	Name	RA (J2000.0)	Dec. (J2000.0)	Net counts	<E> (keV)	Identification (offset) (arcsec)
1	J1641139–484553	16 41 13.99	–48 45 53.30	100 ± 10	2.13	2M 16411400-4845528 (0.5)
2	J1641154–484609	16 41 15.43	–48 46 09.72	10 ± 3	2.60	2M 16411539-4846092 (0.6)
3	J1641167–484516	16 41 16.72	–48 45 16.74	26 ± 5	1.92	2M 16411672-4845165 (0.2)
4	J1641169–484546	16 41 16.95	–48 45 46.08	44 ± 7 (v)	1.50	PD 16411695-4845456 (0.4)
5	J1641170–484603	16 41 17.07	–48 46 03.76	118 ± 11	1.84	2M 16411706-4846034 (0.3)
6	J1641175–484601	16 41 17.54	–48 46 01.11	24 ± 5	2.24	2M 16411756-4846008 (0.3)
7	J1641175–484507	16 41 17.54	–48 45 07.36	16 ± 4	1.85	2M 16411752-4845071 (0.3); GSC (ns)
8	J1641177–484519	16 41 17.78	–48 45 19.20	4 ± 2	2.89	2M 16411779-4845190 (0.2)
9	J1641181–484535	16 41 18.14	–48 45 35.04	13 ± 4 (v)	1.80	PD 16411814-4845345 (0.5)
10	J1641184–484628	16 41 18.41	–48 46 28.36	6 ± 3	1.58	2M 16411843-4846281 (0.4)
11	J1641184–484536	16 41 18.46	–48 45 36.78	15 ± 4	1.97	PD 16411846-4845362 (0.6)
12	J1641185–484500	16 41 18.53	–48 45 00.73	41 ± 6 (v)	2.25	2M 16411852-4845004 (0.4)
13	J1641190–484602	16 41 19.06	–48 46 02.52	58 ± 8	1.94	2M 16411905-4846024 (0.2)
14	J1641194–484519	16 41 19.46	–48 45 19.58	145 ± 12 (v)	2.38	2M 16411944-4845194 (0.3)
15	J1641194–484547	16 41 19.46	–48 45 47.78	888 ± 30	1.22	2M 16411945-4845475 (0.3); HD 150135
16	J1641194–484535	16 41 19.47	–48 45 35.15	4 ± 2	1.56	PD 16411945-4845349 (0.2)
17	J1641200–484554	16 41 20.08	–48 45 54.00	21 ± 5	2.00	PD 16412006-4845535 (0.5)
18	J1641201–484523	16 41 20.10	–48 45 23.22	19 ± 5	2.03	2M 16412001-4845231 (0.9)
19	J1641201–484515	16 41 20.15	–48 45 15.27	27 ± 5	1.89	2M 16412012-4845150 (0.4); GSC (ns)
20	J1641204–484546	16 41 20.44	–48 45 46.93	7293 ± 86 (v)	1.42	2M 16412042-4845466 (0.4); HD 150136
21	J1641205–484536	16 41 20.52	–48 45 36.50	6 ± 3	2.46	PD 16412051-4845359 (0.6)
22	J1641209–484559	16 41 20.92	–48 45 59.43	8 ± 3	1.71	2M 16412089-4845590 (0.5)
23	J1641210–484642	16 41 21.02	–48 46 42.00	61 ± 8 (v)	2.32	2M 16412099-4846418 (0.3)
24	J1641210–484521	16 41 21.07	–48 45 21.86	45 ± 7 (v)	1.63	2M 16412106-4845217 (0.2)
25	J1641217–484641	16 41 21.75	–48 46 41.26	137 ± 12 (v)	2.43	2M 16412172-4846411 (0.4)
26a	J1641221–484457	16 41 22.11	–48 44 57.22	224 ± 15 (v)	2.09	2M 16412210-4844570 (0.3); CD–48 11069
26b	J1641222–484454	16 41 22.25	–48 44 54.80	17 ± 4	3.91	PD 16412227-4844547 (0.3)
27	J1641222–484604	16 41 22.26	–48 46 04.32	12 ± 4	1.99	2M 16412220-4846044 (0.6)
28	J1641223–484628	16 41 22.36	–48 46 28.28	17 ± 4	1.81	2M 16412236-4846278 (0.5)
29	J1641224–484537	16 41 22.42	–48 45 37.08	72 ± 9	1.94	2M 16412240-4845369 (0.3)
30	J1641225–484524	16 41 22.51	–48 45 24.42	22 ± 5 (v)	2.17	2M 16412247-4845241 (0.5); GSC (ns)
31	J1641225–484559	16 41 22.59	–48 45 59.68	15 ± 4	2.39	2M 16412258-4845594 (0.3)
32	J1641227–484535	16 41 22.77	–48 45 35.32	20 ± 5	2.04	2M 16412276-4845350 (0.3)
33	J1641232–484449	16 41 23.27	–48 44 49.70	16 ± 4	1.78	2M 16412327-4844494 (0.3); GSC (s) R = 16.5
34	J1641234–484604	16 41 23.46	–48 46 04.37	144 ± 12 (v)	2.21	2M 16412343-4846041 (0.4)
35	J1641238–484520	16 41 23.84	–48 45 20.85	46 ± 7 (v)	1.82	2M 16412383-4845206 (0.2); GSC (ns)
36	J1641242–484543	16 41 24.26	–48 45 43.83	32 ± 6	1.87	2M 16412425-4845436 (0.2)
37	J1641244–484552	16 41 24.40	–48 45 52.78	52 ± 7	1.99	2M 16412440-4845524 (0.3); NGC6193-9
38	J1641247–484534	16 41 24.73	–48 45 34.68	25 ± 5	1.67	2M 16412471-4845345 (0.3)
39	J1641247–484545	16 41 24.75	–48 45 45.13	15 ± 4	1.51	2M 16412475-4845452 (0.1)
40	J1641256–484619	16 41 25.60	–48 46 19.28	32 ± 6 (v)	1.60	2M 16412558-4846189 (0.4); GSC (s) R = 16.7
41	J1641258–484514	16 41 25.88	–48 45 14.51	44 ± 7	0.87	2M 16412586-4845142 (0.3); CD–48 11071
42	J1641262–484548	16 41 26.28	–48 45 48.91	19 ± 4 (v)	1.76	2M 16412625-4845487 (0.4)

Notes: Sources detected by the CIAO *wavdetect* algorithm within a $2.1' \times 2.1'$ region centered on HD 150136 are included in this table. Net counts from *wavdetect* were accumulated in ACIS-S 0th order images during an exposure live time of 90,337 secs and are background subtracted. Dispersed counts in the MEG and HEG grating arms are not included in the net counts quoted above for HD 150135 and HD 150136. Sources 8 and 16 are marginal X-ray detections. Sources 26a,b are a close pair separated by $2.8''$. A “(v)” following net counts indicates that the source is likely variable with a probability of constant count rate $P_{\text{const}} < 0.05$ as determined from the KS statistic using source events in the 0.5 - 7.0 keV range. <E> is the mean photon energy using source events in the 0.5 - 7.0 keV range. Infrared identifications are from 2MASS (2M) and Pico dos Dias (PD) images. The offset between X-ray and IR positions is given in parentheses. Sources with optical counterparts within $1''$ of the X-ray position in the *HST* Guide Star Catalog are denoted as GSC (s) if the GSC classification is stellar and GSC (ns) if non-stellar. The GSC R magnitude is given if stellar.

Table 3. Chandra Spectral Fit Results

Parameter	HD 150135	HD 150136
Spectrum	MEG1	MEG1
Net counts (MEG)	1098	8780
Model	2T bvapec	2T bvapec
N_H (10^{21} cm^{-2})	[4.0]	[4.0]
kT_1 (keV)	0.23 ± 0.10	0.35 ± 0.04
kT_2 (keV)	0.57 ± 0.25	1.00 ± 0.07
EM_1 (10^{56} cm^{-3})	0.90	2.29
EM_2 (10^{56} cm^{-3})	0.13	0.62
FWHM (km s^{-1})	2423 ± 1692	2547 ± 182
Abundances	varied ^a	varied ^b
χ^2/dof	9.5/44	242.1/383
χ^2_{red}	0.22	0.63

^aBest-fit HD 150135 abundances relative to the solar values of Anders & Grevesse (1989) and 90% confidence errors were: O = 0.45 (+0.75, -0.39), Ne = 0.40 (± 0.31), Mg = 0.33 (± 0.30), Si = 0.47 (+0.63, -0.37), Fe = 0.35 (± 0.25); all other elements fixed at solar values.

^bBest-fit HD 150136 abundances relative to the solar values of Anders & Grevesse (1989) and 90% confidence errors were: O = 0.35 (± 0.20), Ne = 0.33 (± 0.09), Mg = 0.56 (± 0.11), Si = 0.77 (± 0.12), S = 1.10 (± 0.44), Fe = 0.20 (± 0.06); all other elements fixed at solar values.

Notes: Based on fits of the MEG 1st order spectra binned to a minimum of 20 counts per bin (Figs. 8 - 9) using an absorbed 2T *bvapec* optically thin plasma model in XSPEC v. 11.3.1. The tabulated parameters are absorption column density (N_H), plasma temperature (kT), emission measure (EM), and the best-fit line width (FWHM). Errors are 90% confidence. $N_H = 4.0 \times 10^{21} \text{ cm}^{-2}$ was held fixed during fitting at the value derived from $E(B-V) = 0.48 - 0.49$ and $R = A_V/E(B-V) = 3.5$ (HH77) using the conversion formula of Gorenstein (1975). If N_H is varied, the higher S/N spectrum of HD 150136 gives a 90% confidence range $N_H = [3.4 - 6.0] \times 10^{21} \text{ cm}^{-2}$.

Table 4. HD 150136 X-ray Line Properties

Ion	Inst.	λ_{lab} (Å)	λ_{obs} (Å)	$\Delta\lambda$ (mÅ)	FWHM (mÅ)	FWHM (km/s)	Flux	R	G	T_{max} (K)	R_c (R_*)
S XV	HEG	5.0387	5.0351 ± 0.011	-3.6	33^{+28}_{-8}	1965^{+833}_{-534}	$1.26^{+1.27}_{-0.94}$	$1.6^{+0.5}_{-1.5}$	$0.9^{+3.8}_{-0.8}$	7.2	1.7
Si XIV	HEG	6.1804	6.1816 ± 0.005	+1.2	38^{+11}_{-8}	1844^{+534}_{-388}	$1.02^{+0.22}_{-0.22}$	7.2	...
Si XIII	HEG	6.6479	6.6482 ± 0.006	+0.3	43^{+12}_{-8}	1940^{+541}_{-361}	$4.01^{+0.85}_{-1.70}$	$1.0^{+0.9}_{-0.4}$	$0.9^{+0.4}_{-0.3}$	7.0	3.9
Mg XII	HEG	8.4192	8.4163 ± 0.004	-2.9	42^{+9}_{-7}	1496^{+321}_{-249}	$1.44^{+0.29}_{-0.29}$	7.0	...
Mg XI	HEG	9.1687	9.1688 ± 0.005	+0.1	76^{+16}_{-11}	2487^{+524}_{-360}	$7.15^{+1.35}_{-1.35}$	$0.6^{+0.4}_{-0.3}$	$0.6^{+0.3}_{-0.5}$	6.8	10.1
Ne X	HEG	12.1321	12.1288 ± 0.010	-3.3	92^{+18}_{-15}	2275^{+445}_{-371}	$6.80^{+1.17}_{-1.17}$	6.8	...
Ne IX	MEG	13.4473	105^{+15}_{-12}	2342^{+335}_{-268}	$10.3^{+1.70}_{-1.70}$	$0.2^{+0.2}_{-0.1}$	$1.0^{+0.3}_{-0.3}$	6.6	30.7
O VIII	MEG	18.9671	18.9692 ± 0.012	+2.1	176^{+21}_{-21}	2784^{+332}_{-332}	$11.2^{+1.50}_{-1.50}$	6.5	...
O VII	MEG	21.6015	21.5998 ± 0.032	-1.7	121^{+53}_{-32}	1680^{+736}_{-444}	$6.70^{+4.14}_{-3.16}$	$\leq 0.1^{+0.4}_{-0.1}$	$1.2^{+2.9}_{-0.8}$	6.3	116.

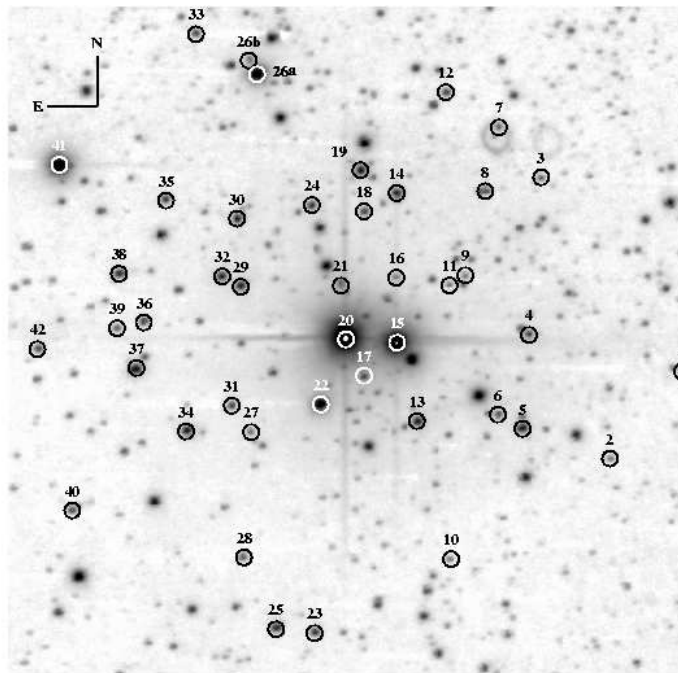
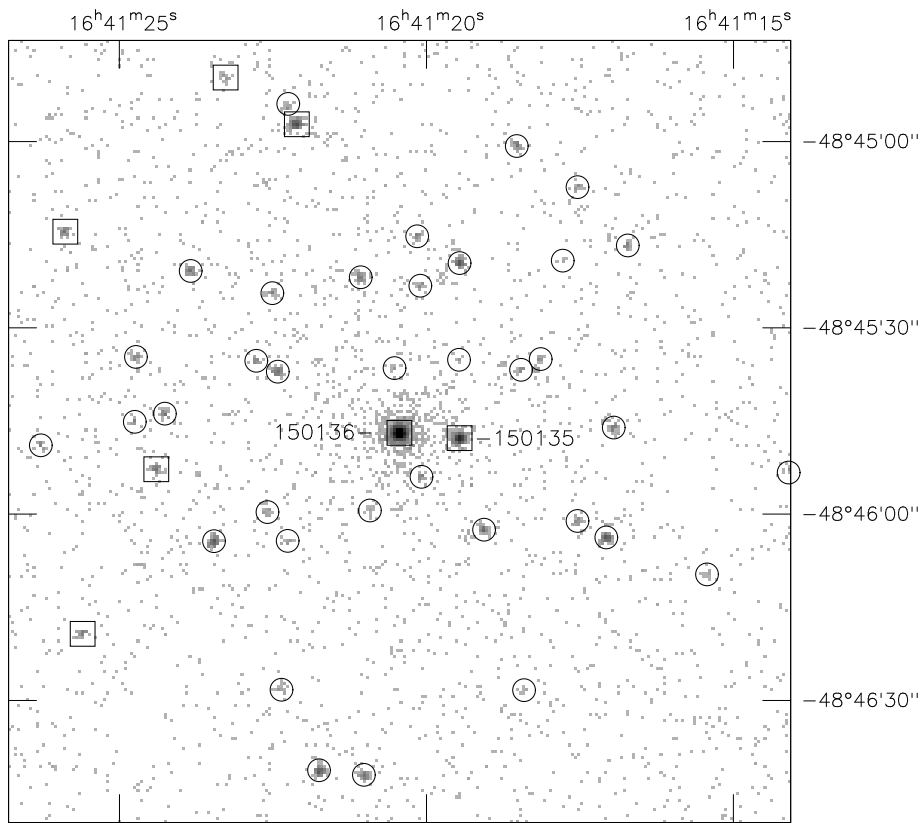
Notes: Data are from Gaussian fits of first-order grating spectra. $\Delta\lambda = \lambda_{obs} - \lambda_{lab}$, where λ_{lab} is the rest wavelength from ATOMDB v. 1.3.1 and λ_{obs} is the observed (best-fit) wavelength. Line flux units are 10^{-5} ph cm $^{-2}$ s $^{-1}$. Errors are $\pm 1\sigma$. For He-like triplets, λ_{obs} is for the resonance (*r*) line, and fluxes are the sum of contributions from the resonance (*r*), intercombination (*i*), and forbidden (*f*) lines. Flux ratios are $R = f/i$ and $G = (f + i)/r$. In the low-density limit, $R \rightarrow R_0$, where $R_0 = 2.04$ (S XV), 2.51 (Si XIII), 3.03 (Mg XI), 3.17 (Ne IX), 3.85 (O VII) (Blumenthal et al. 1972). For Ne IX, the wavelength was held fixed at λ_{lab} during fitting do to blending from nearby Fe lines. The O VII line is faint and measurements have large uncertainties. T_{max} is the log temperature of maximum line power from ATOMDB. R_c for He-like triplets is the critical radius (in units of stellar radii) where the photoexcitation rate from the upper level of the *f* transition is equal to the spontaneous decay from that level, computed using the procedure of Kahn et al. (2001). Quoted values of R_c assume a spectral type of O3V and blackbody spectra with $T_{eff} = 51230$ K (Vacca et al. 1996). The R_c values for O3I are $\approx 1\%$ less.

Table 5. Adopted O Star Parameters

Spectral type	M^a (M_\odot)	R^a (R_\odot)	$\log \dot{M}$ ($M_\odot \text{ yr}^{-1}$)	v_∞^c (km s^{-1})
O3I	64.4	17.8	-4.9^d	3150
O3V	51.3	13.2	-5.7^b	3190
O6V	33.1	10.7	-6.0^d	2570
O6.5V	30.8	10.3	-6.2^b	2455

^aVacca et al. 1996^bGarmany et al. 1981^cPrinja et al. 1990^dLamers & Leitherer 1993

NGC 6193 (Chandra ACIS-S)



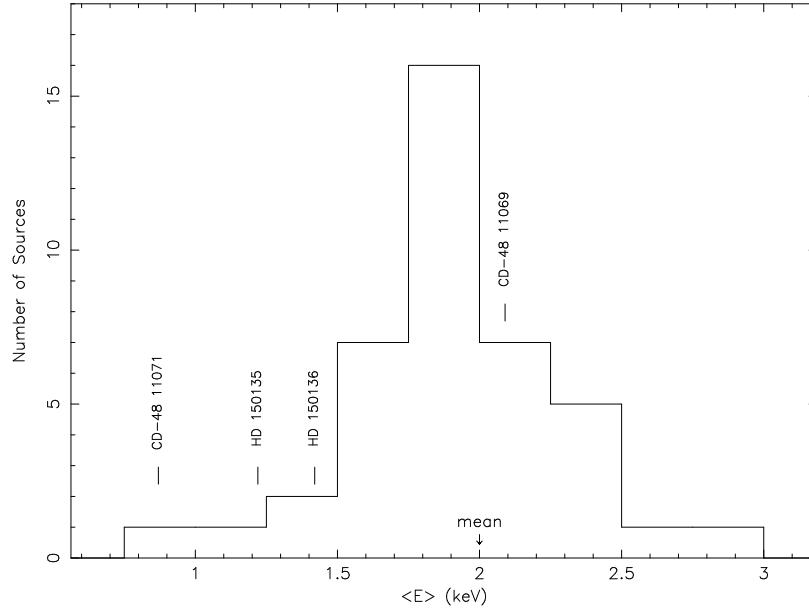


Figure 2. Distribution of the mean photon energy $\langle E \rangle$ for the 43 X-ray sources detected in the central region of NGC 6193. Three OB stars shown have soft energy distributions, but the B0-1 star CD -48 11069 has an above average $\langle E \rangle$ that may be due to a low-mass companion.

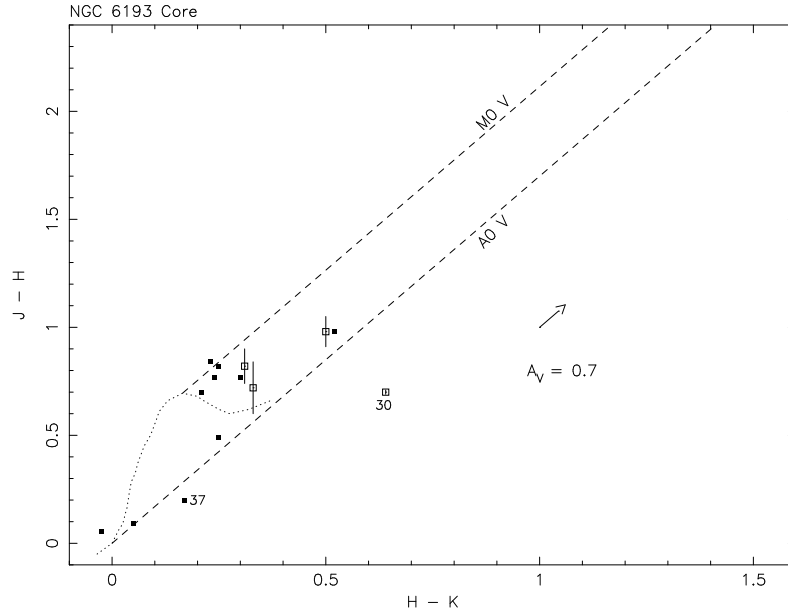


Figure 3. Near-IR color-color diagram for central region of NGC 6193. Solid squares show 2MASS colors of 10 X-ray sources whose 2MASS JHK magnitudes do not have confusion flags (X-ray sources 1, 5, 23, 25, 26a, 34, 35, 37, 38, 41). Open squares show 2MASS colors of four sources which have a confusion flag at J band, but not at H or K (X-ray sources 2,3, 28, 30). The unreddened zero-age main sequence is shown as a dotted line at lower left. The two sloping dashed lines mark the approximate reddening band for M0 V and A0 V stars using data from Bessell & Brett (1988) and Rieke & Lebofsky (1985). The reddening vector corresponds to foreground reddening $E(B-V) = 0.2$ mag and $A_V = 3.5 \times E(B-V) = 0.7$ mag (HH77).

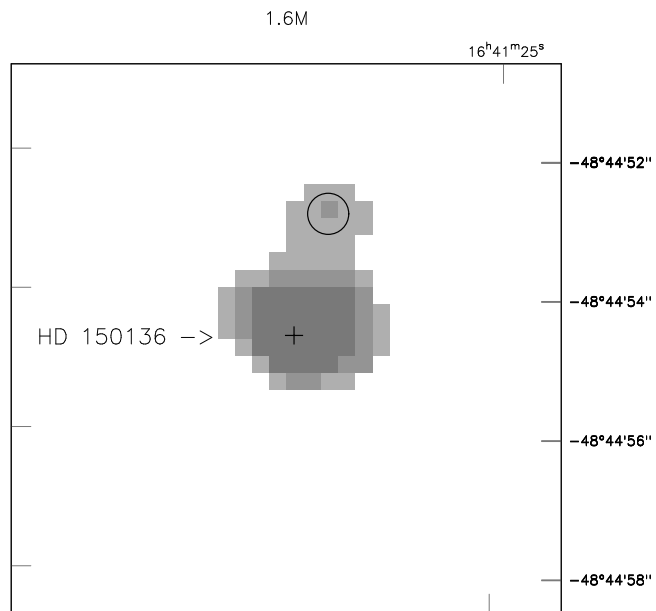


Figure 4. Pico dos Dias 2.14 μm image of HD 150136, showing the faint IR companion 1.7'' to its north.

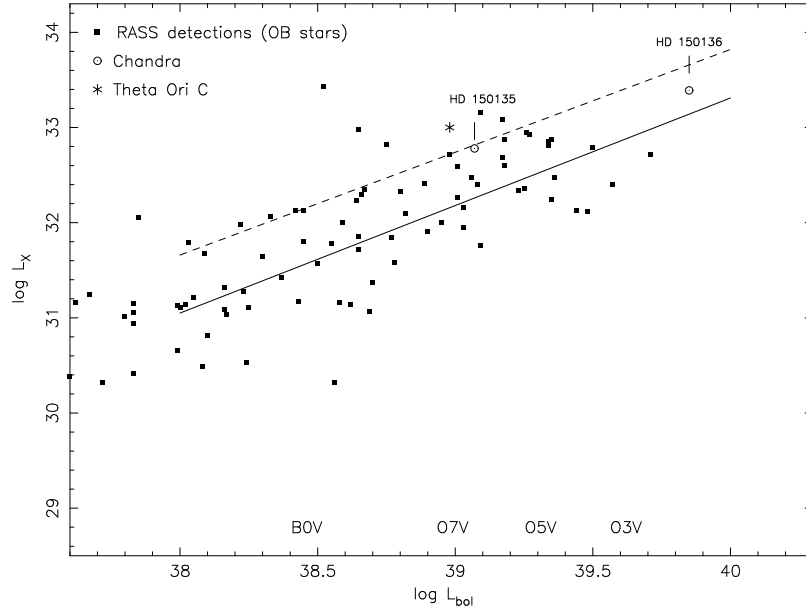


Figure 5. L_X versus L_{bol} for luminous OB stars detected in the RASS (solid squares) as catalogued by Berghöfer et al. (1996). Upper limits for undetected OB stars in the RASS are not shown. Circled symbols are *Chandra* data. For comparison, the asterisk shows the young magnetic star θ^1 Ori C (O7V) using L_{bol} from Hillenbrand (1997) and L_X from the *Chandra* HETG analysis of Gagne et al. (2005). Solid line is the regression fit derived for RASS OB stars, accounting for non-detections, by Berghöfer et al. (1997). Dashed line is the regression fit for O stars determined in the *Einstein* study of Sciortino et al. (1990).

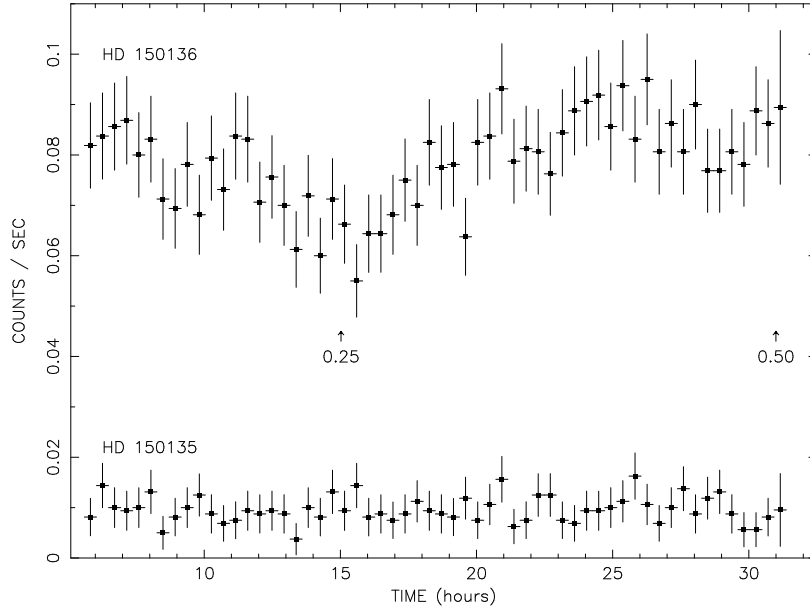


Figure 6. Zeroth order *Chandra* ACIS-S light curves of HD 150135 and HD 150136 in the 0.5 - 5 keV band, binned at 1600 s intervals. Time (hours) is referenced to 00:00 UT on 27 June 2002. The observation began at 05:20 UT. Arrows mark HD 150136 orbital phases $\phi = 0.25$ and $\phi = 0.50$ as determined from the ephemeris of Niemela & Gamen (2005). Absorption features from a possible third star in the system appear in optical spectra at $\phi = 0.25$. The primary moves in front at $\phi = 0.50$.

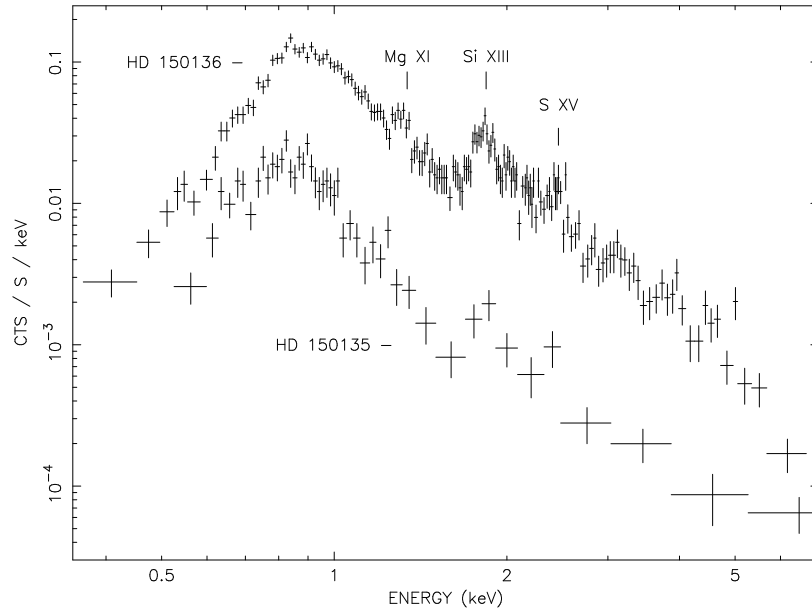


Figure 7. Background-subtracted 0th order *Chandra* ACIS-S spectra of 150135 and HD 150136.

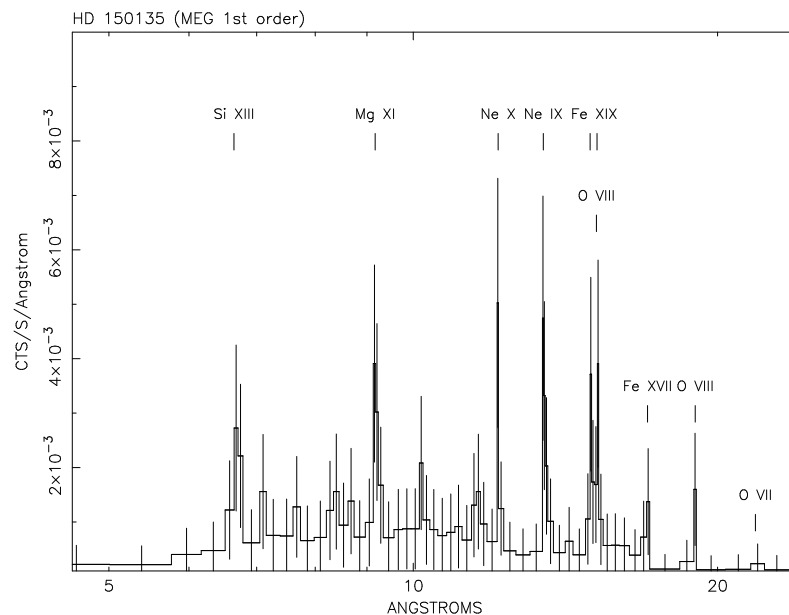


Figure 8. *Chandra* 1st order background-subtracted MEG spectrum of HD 150135. The +1 and -1 orders have been co-added.

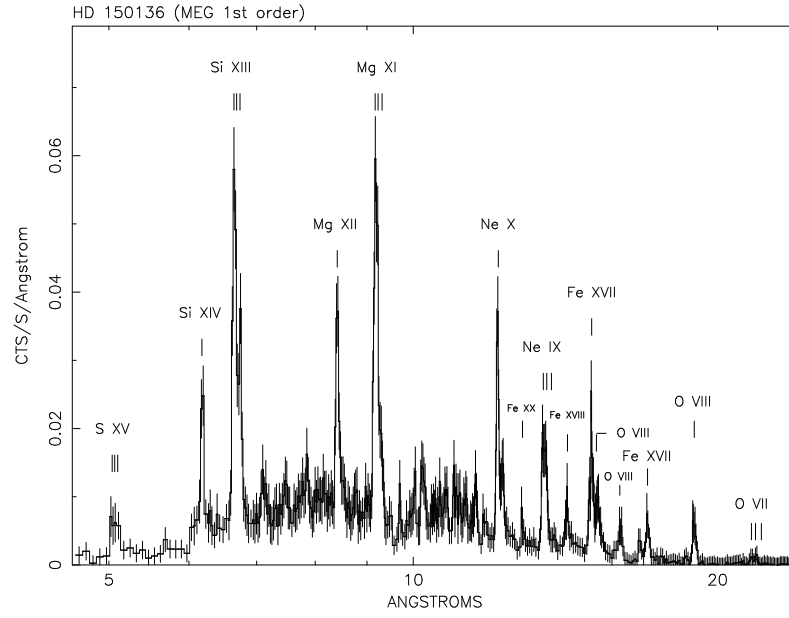


Figure 9. *Chandra* 1st order background-subtracted MEG spectrum of HD 150136. The +1 and −1 orders have been co-added.

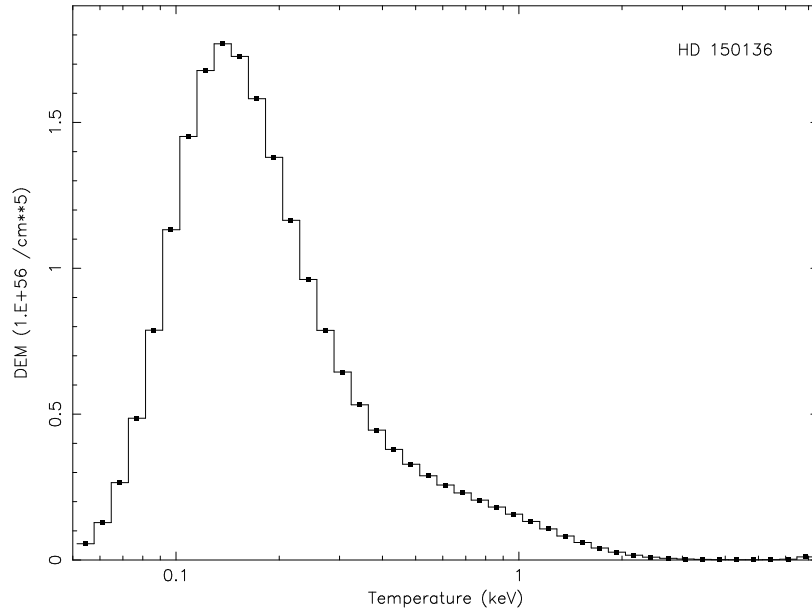


Figure 10. Differential emission measure (DEM) distribution of HD 150136. The DEM was derived using a Chebyshev polynomial algorithm (see text).

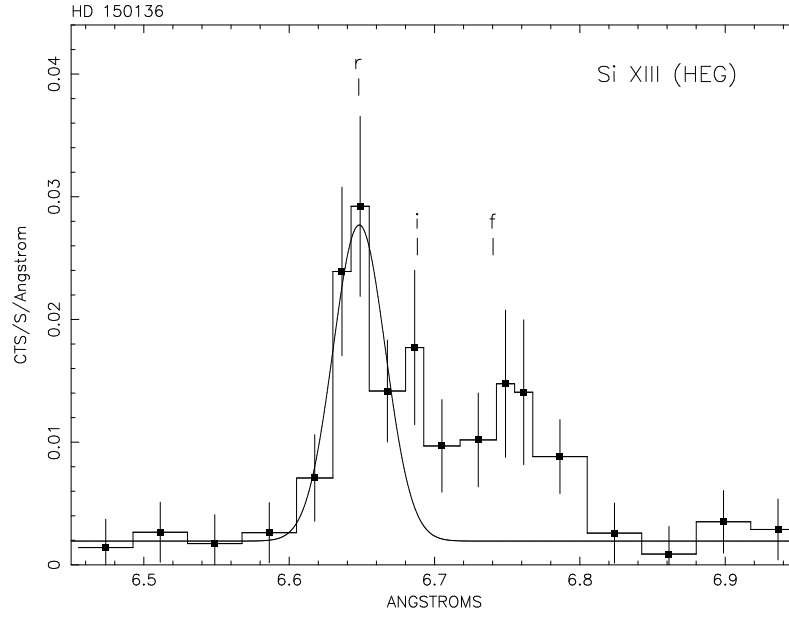


Figure 11. Si XIII He-like triplet of HD 150136 from the background-subtracted 1st order *Chandra* HEG spectrum. The +1 and −1 orders have been co-added. The Gaussian fit of the resonance (*r*) line has FWHM = 42.3 mÅ.

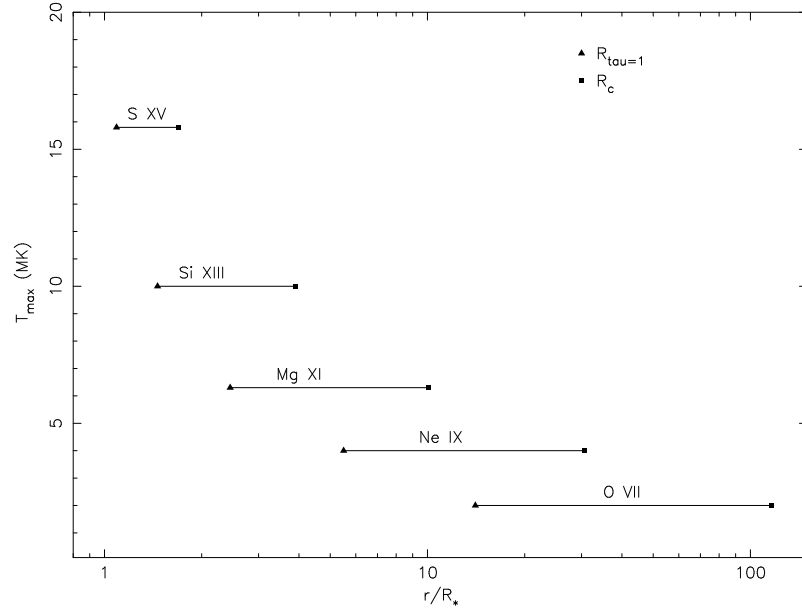


Figure 12. Radius of optical depth unity ($R_{\tau=1}$) and critical photexcitation radius R_c (Table 4) for He-like triplets in HD 150136. T_{max} is the temperature at which line power is maximum. The adopted stellar parameters are for O3V (Table 5). The value of $R_{\tau=1}$ is calculated using solar abundance cross sections (Balucinska-Church & McCammon 1992) and assumes a spherically symmetric homogeneous wind. The values of $R_{\tau=1}$ for non-solar abundances derived from X-ray spectral fits (Table 3) are smaller by factors ranging from 6% for S XV to 29% for Ne IX and O VII. The solid lines connecting the two radii represent the interval over which the lines could form under the constraints $r > R_{\tau=1}$ and $r < R_c$, where the latter follows from UV suppressed R ratios (see text).

This paper has been typeset from a \TeX / \LaTeX file prepared
by the author.